Journal Pre-proofs

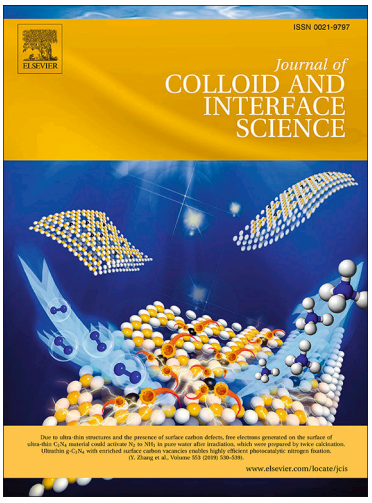

Electromagnetic performance, Optical and Physiochemical Features of $CaTiO_3$/NiO and $SrFe_{12}O_{19}$/NiO Nanocomposites Based Bilayer Absorber

Li Feng, Jiajun Liu, Isabelle Huynen, Mustafa Z. Mahmoud, Majid Niaz Akhtar

PII: S0021-9797(21)02041-5
DOI: https://doi.org/10.1016/j.jcis.2021.11.127
Reference: YJCIS 29268

To appear in: *Journal of Colloid and Interface Science*

Received Date: 15 October 2021
Revised Date: 16 November 2021
Accepted Date: 21 November 2021

Please cite this article as: L. Feng, J. Liu, I. Huynen, M.Z. Mahmoud, M. Niaz Akhtar, Electromagnetic performance, Optical and Physiochemical Features of $CaTiO_3$/NiO and $SrFe_{12}O_{19}$/NiO Nanocomposites Based Bilayer Absorber, *Journal of Colloid and Interface Science* (2021), doi: https://doi.org/10.1016/j.jcis.2021.11.127

Electromagnetic performance, Optical and Physiochemical Features of $CaTiO_3$/NiO and $SrFe_{12}O_{19}$/NiO Nanocomposites Based Bilayer Absorber

Li Feng[1,*], Jiajun Liu[1], Isabelle Huynen[2], Mustafa Z. Mahmoud[3,4], Majid Niaz Akhtar[5,*]

Authors Statement

Conceptualization: Li Feng, Majid Niaz Akhtar
Methodology: Jiajun Liu,
Validation: Mustafa Z. Mahmoud,
Investigation: Jiajun Liu,
Writing—original draft preparation: Li Feng, Isabelle Huynen, Majid Niaz Akhtar,
Writing—review and editing: Li Feng, Isabelle Huynen, Majid Niaz Akhtar
Supervision and Funding Acquisition: Li Feng, Mustafa Z. Mahmoud

1- School of Civil and Transportation Engineering, Guangdong University of Technology, Guangzhou 510006, Guangdong, China
2- ICTEAM Institute, ELEN Division, Place du Levant 3, Louvain-la-Neuve B-1348, Belgium
3-Department of Radiology and Medical Imaging, College of Applied Medical Sciences, Prince Sattam bin Abdulaziz University, Al-Kharj 11942, Saudi Arabia
4- Faculty of Health, University of Canberra, Canberra, ACT, Australia.
5- Department of Physics, Muhammad Nawaz Sharif University of Engineering and Technology, Multan 60000 Pakistan

Corresponding authors email:

Majid Niaz Akhtar: majidniazakhtar@mnsuet.edu.pk, majidniazakhtar@gmail.com

Li Feng: fl19860314@126.com

Graphical Abstract

Structural, Microstructure and RL curves of Single and Double Layers Absorbers of D and D/M samples

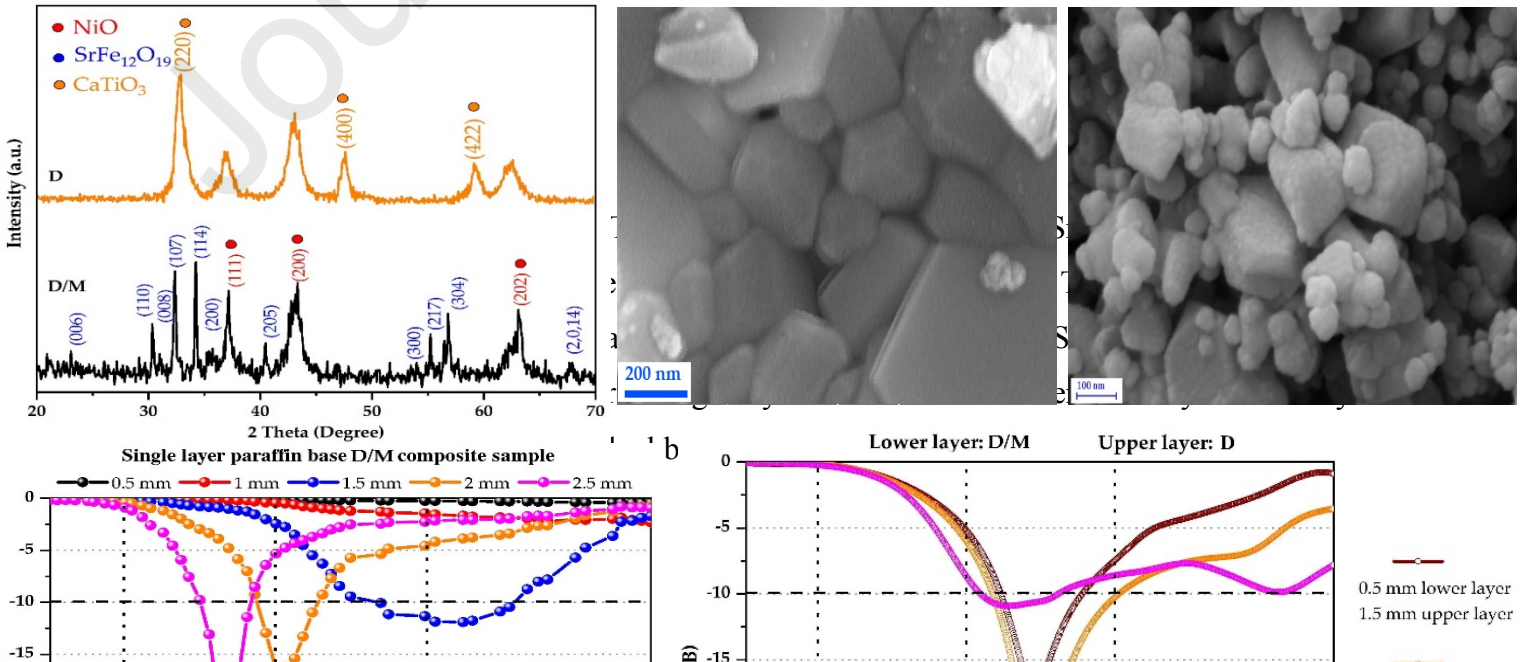

analysis after finding the appropriate thickness of each layer. The reflection loss from each single layer samples containing 20 wt.% of each $CaTiO_3$/NiO and $SrFe_{12}O_{19}$/NiO nanocomposites were -16 dB and -35 dB at 6.3 GHz with 2.5 mm matching thickness respectively. However, the RL was -34 dB at 10 GHz frequency with 2 mm thickness in a bilayer absorber with $SrFe_{12}O_{19}$/NiO nanocomposite layer put as absorbing layer with 1 mm thickness and $CaTiO_3$/NiO positioned as matching layer with 1 mm thickness. Furthermore, at the X-band frequency, approximately entire band absorption is obtained. The findings demonstrate that adjusting the order and thickness of the layers in a bilayer absorber may readily improve microwave absorption performance. By comparing the results of simulation with real prepared bilayer absorbers, we found that with a 2 mm overall thickness, the bi-layer absorbers display accurate RL values, but not the matching frequency monitored in the simulation process. In reality, this discrepancy was unavoidable.

Keywords: Bilayer Absorber, $CaTiO_3$, $SrFe_{12}O_{19}$, NiO, CST suite.

1. Introduction

Efficient MAS (microwave absorbing structures) are developed as protection against electromagnetic interferences, as stated in [1,2]. Polymer composites hosting conductive charges combine high conductivity, mechanical rigorousness as well as prospects of conformability. MAS designed for stealth applications decreased RCS the (radar cross-section) of many objects. The absorbing layer used by MAS in 8–12.4 GHz radar communications is very much needed [3-5]. Carbon based materials including single and multilayer arrangements produce reflection below −10 dB [6,7]. A good absorber must have minimum reflection from signal incidence to its surface and have maximum absorption from thickness. In order to counterbalance the reflective effect of highly conductive charges, incorporation of magnetic charges in the composite is a good strategy [8–11]. This may decrease the reflection at the input interfaces. However, the absorption is also preferred over the diffusion of the signal. Modification of filler structure, their weight percent, absorber structure design are the focus of the majority of research in the development of MAM absorbers. [12-16].

In the current project, we explored the absorption capability of $CaTiO_3$ or $SrFe_{12}O_{19}$ nanoparticles both decorated with TiO_2 oxide. As reported in the literature, calcium titanate and strontium hexaferrite have already been investigated for microwave absorption. In [17] nanocrystalline calcium titanate was synthetized using hydrothermal method, and then dispersed in epoxy resin for characterization in the X and Ku bands. Best minimal RL of - 30 dB (i.e. frequency range where RL < -10 dB) of 2.2 GHz around 9 GHz was obtained for epoxy sample 1 mm-thick. $CaTiO_3$ was synthetized using hydrothermal method and dispersed in epoxy slab 2.8 mm-thick, for achieving RL (-14 dB) around 11 GHz [18]. A mix of strontium and iron salts were precipitated, annealed and compressed as compact powder molded into slab; best performances were obtained for a slab thickness of 3.5 mm and around 9.2 GHz, with RL = -23 dB and a 10dB bandwidth equal

to 3.4 GHz [19]. Ultrathin $SrFe_{12}O_{19}$ nanosheets were prepared using hydrothermal route. RL of - 28.6 dB with bandwidth of 10 dB was obtained at 0.92 GHz having 3.5 mm thickness of the absorber [20]. Sr hexaferrite and zinc ferrite with different wt. ratios were prepared. The reflection loss of -37 dB was investigated for 2.2 mm thickness [21]. Ternary nanocomposites of rGO/Sr ferrite/polyaniline were fabricated for absorption purpose. The resulting product shows the best absorption for 1.5 mm thickness in 2–18 GHz. The minimum RL value was −45 dB at 16.08 GHz with 5.48 GHz as 10 dB bandwidth [22]. Calcium titanate was also combined with $ZnFe_2O_4$ in bilayered configuration [31]. According to the result, the reflection loss value for a 2 mm single layer absorber sample with 20 wt.% of [CT/ZF]@C was -22 dB. But when a bilayer absorber is prepared by using 0.5 mm of non-filled resin based layer at the top layer, the absorption layer is reduced to 1.5 mm, the absorption performance improves and the reflection loss value increases to -24 dB with whole band absorption.

Section 2 of our paper describes the synthesis methods for $CaTiO_3$ and $SrFe_{12}O_{19}$ nanocomposites, as well as their physico-chemical, morphological and electromagnetic characterization tools. Section 3 discusses the results provided by FTIR, XDR, BET, UV, XPS, FESEM and EDX images, and studies the microwave behavior of our two nanocomposites. The reflection losses are evaluated by varying the frequency and thickness of the composite sample, for monolayer topology or bilayer topology combining $CaTiO_3$ and $SrFe_{12}O_{19}$.

2. Materials and methods

2.1. Preparation of Calcium titanate micro-cubes/NiO nanocomposite (D)

Hydrothermal method was utilized as chemical method to synthesize micro-cubes calcium titanate powder from $TiCl_4$, $CaCl_2.2H_2O$ and KOH as raw precursors. Three distinct solutions were prepared simultaneously, in the first one $TiCl_4$ dissolved in pre-cooled deionized water, in the second on $CaCl_2.2H_2O$ dissolved in deionized water and in the third one KOH which acted as a mineralizer dissolved in deionized water for preparing 8 M KOH solution. Two solutions containing Ti^{4+} and Ca^{2+} ions were completely mixed and stirred for 1 h and then KOH solution added drop-wisely to the as-prepared suspension and the pH value reached to 14. Finally, the prepared sample was shifted into Teflon lined hydrothermal autoclave reactor and kept at 210 °C for 6 h. The final powder was centrifuged, dried and sintered at 700 °C for 2 h.

In the next step, as-prepared $CaTiO_3$ powder and a certain volume of NH4OH were liquified in deionized water and stirred for 15 min. Then $NiCl_2$ is added to the above mixture (weight ratio of $CaTiO_3$: NiO was considered 50:50 wt.%) and stirred for 1 h. The resulting mixture was placed in the autoclave and heated for 10 h at 160°C. The obtained powder was centrifuged, rinsed, dried, and sintered for 1 hour at 400 ° C.

2.2. Preparation of $SrFe_{12}O_{19}$/NiO nanocomposite (D/M)

Initially, iron nitrate and strontium nitrate salts as raw precursors without further purification were dissolved into mixture of deionized water and ethanol with an equal volume ratio. After magnetically stirring for 1 h, the pH value was tuned to 14 using 6 M KOH solution. The prepared solution was sealed and maintained at 200 °C for 24 h in an autoclave. The resultant dark brown centrifuged powders were rinsed and then dried at 90 °C for 8 h. The prepared powder was sintered in an air environment at 900°C for 2 h.

$SrFe_{12}O_{19}$/NiO nanocomposite is prepared just as the above process in section 2.1.

2.3. Characterizations

X-ray diffractometer (XRD, Philips -PW1730), FTIR (Perkin-Elmer RXI FTIR Spectrometer), X-ray photoelectron analysis (XPS, KRATOS), field-emission scanning electron microscopy (FESEM, ZEISS), UV–Vis light absorption (Shimadzu), Brunauer-Emmett-Teller (BET, Microtrac Bel) and vector network analyzer (VNA, Agilent PNA N5244A) were used to assess structures and morphological characteristics. To apply the coaxial characterization approach described in [23], the VNA sample tests were prepared into a ring shape.

2.4. Fabrication of Absorbers

Monolayer coaxial absorbers were prepared in the first step with 20 wt. percent of both nanocomposites in paraffin base matrix, and electromagnetic parameters, as well as reflection losses RL, were measured using VNA analysis to simulate the microwave absorption properties of a bilayer absorber. The absorption properties of bilayer absorbers were simulated using CST studio. Following the simulation and determination of the ideal thickness condition for each layer, a double layer paraffin base absorber sample with the optimal thickness is created and the results are compared to the simulation results.

3. Results and discussion

3.1 Physico-chemical characterization

3.1.1 XRD and FTIR analysis

Figure 1 illustrates the XRD patterns of $CaTiO_3$/NiO and $SrFe_{12}O_{19}$/NiO samples. XRD patterns of each sample are comprised by two distinct phases. In other words, in addition to the characteristic peaks of $CaTiO_3$ and $SrFe_{12}O_{19}$ in $CaTiO_3$/NiO and $SrFe_{12}O_{19}$/NiO samples respectively, new broad diffraction peaks were observed at 37.5°, 43.5° and 63.2° which related to pure NiO nanoparticles decorated on both $CaTiO_3$ and $SrFe_{12}O_{19}$ particles. Three main diffraction peaks of $CaTiO_3$ phase are centered at 33.2°, 47.2° and 59.1°which were

assigned to the (220), (400), (422) crystal planes respectively. Moreover, for $SrFe_{12}O_{19}$ phase, all characteristic peaks were assigned to their crystal planes and there were no impurity peaks.

FTIR spectra of $CaTiO_3$/NiO and $SrFe_{12}O_{19}$/NiO samples is shown in Figure 1b. The absorption bands which are existing in the range of 700-400 cm^{-1} represented the metal oxide (M-O) stretching bonds of octahedral and tetrahedral sites in the $CaTiO_3$/NiO and $SrFe_{12}O_{19}$/NiO samples [24]. The higher frequency bands appear at 641 and 656 cm^{-1} depicted the tetrahedral sites in the samples. However, the lower frequency band at 578 and 579 cm^{-1} shows octahedral sites of metal cations in $CaTiO_3$/NiO and $SrFe_{12}O_{19}$/NiO samples. The bands at 1491, 1629 and 1689 cm^{-1} show the presence of the benzenoid and quinoid rings in composite samples [25]. The peak at 3651 and 3500 cm^{-1} depicted the presence of N-H bonding in the prepared composite samples.

The peaks at 1689 and 3651 cm^{-1} depicted the O – H deformation vibration and stretching vibration of adsorbed water molecules in $CaTiO_3$@NiO sample. Furthermore, the peaks at 431 and 579 cm-1 corresponded to the Ti–O stretching vibration and Ti–O–Ti bridging stretching modes, which are connected to the environment around the TiO6 octahedral structure. Moreover, the peak at 656 cm^{-1} depicted the Ni – O stretching vibration mode whereas the peak at 1491 cm^{-1} shows the bending vibration of TiO_3^{-2}in $CaTiO_3$/NiO sample. For $SrFe_{12}O_{19}$@NiO sample, the peaks at 1629 and 3500 cm^{-1} shows the O – H deformation vibration and stretching vibration mode of water molecules. The peaks at 578 and 641 cm^{-1} shows the Fe – O and Ni – O stretching vibration. Further, the peaks at 1104 cm^{-1} are attributed to the Fe – O – Ni stretching vibration which proves that NiO successfully deposited on strontium hexaferrite.

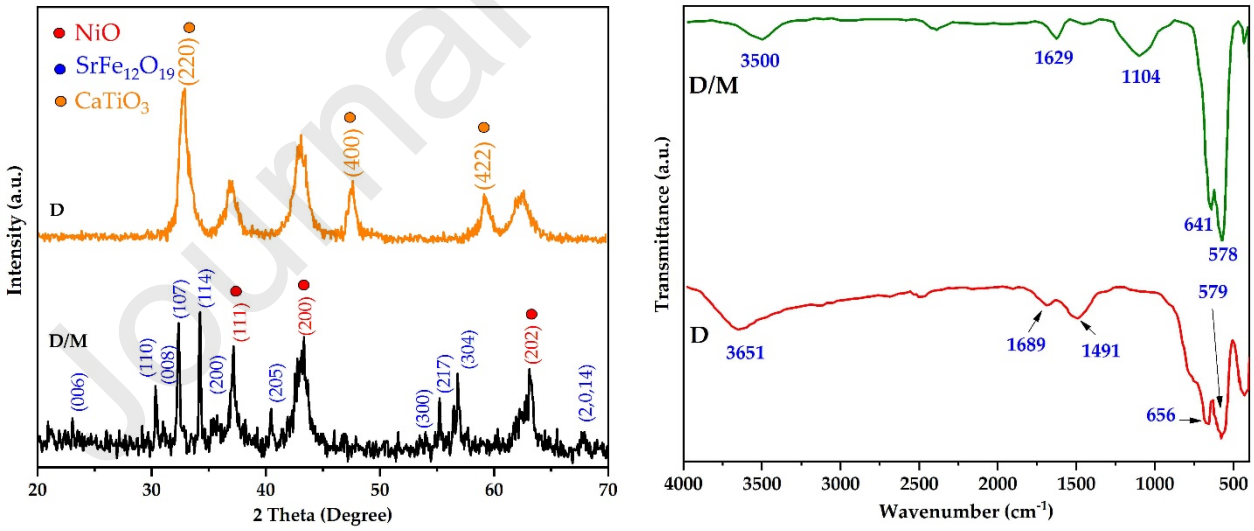

(a) (b)

Figure 1. a) XRD and b) FTIR analysis results of as-prepared D and D/M samples.

3.1.2 XPS analysis

Surface chemical states of the $CaTiO_3$/NiO and $SrFe_{12}O_{19}$/NiO nanocomposites were determined using XPS analysis. The wide survey scan XPS spectra of $CaTiO_3$/NiO sample (Figure 2a) clearly illustrate the presence of C, Ca, Ti, O and Ni elements. Sr3d, C1s, O1s, Fe2p and Ni2p peaks were observed in XPS spectra of $SrFe_{12}O_{19}$/NiO sample (Figure 2b). The peaks observed at 358.9 eV and 347.2 (Figure 2a) are ascribed to Ca $2p_{1/2}$ and Ca $2p_{3/2}$ respectively. Also, the presence of +4 oxidation state of Ti in $CaTiO_3$ confirmed by two peaks at 464.9 eV (Ti $2p_{1/2}$) and (459.2 (Ti $2p_{3/2}$) Fig. 2a). The peaks at 133.3 and 135.0 eV can be related to Sr $3d_{5/2}$ (arose from Sr-O chemical bond) and Sr $3d_{3/2}$ (arose from the presence of Sr^{2+}), respectively. Moreover, the presence of Fe^{3+} ions in $SrFe_{12}O_{19}$ confirmed by the appearance of Fe 2p peaks at 711.6 eV (Fe $2p_{3/2}$) and 736.2 eV (Fe $2p_{1/2}$) binding energy. Also in both spectra the appearance of Ni $2p_{1/2}$ at 873.8 eV and Ni $2p_{3/2}$ at 856.2 eV binding energy, confirmed the formation of nickel oxide phase in both samples. The results were perfectly consistent with the XRD results in Figure 1a.

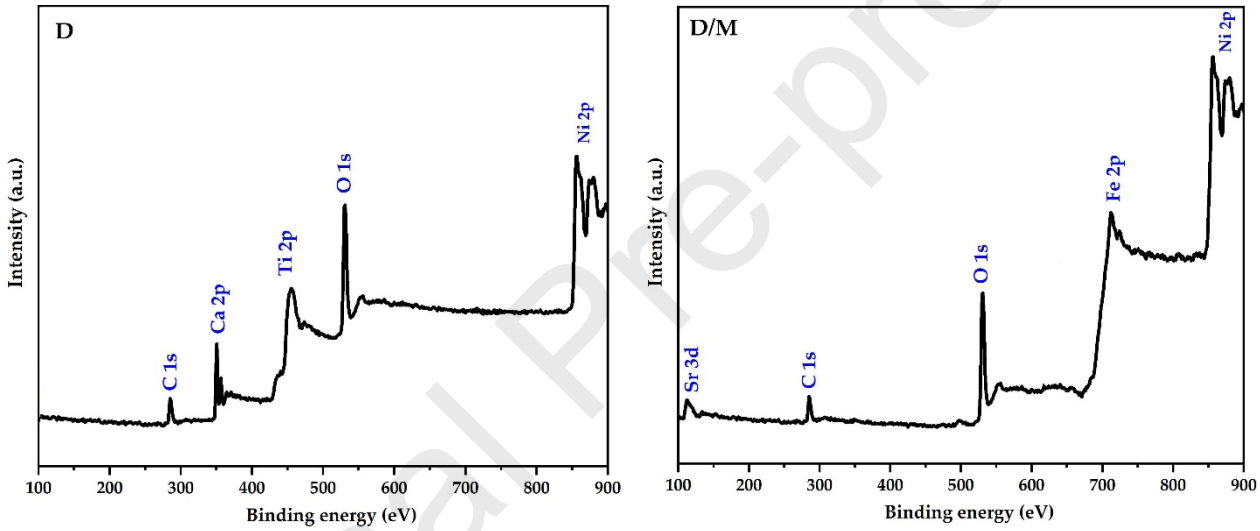

(a) (b)

Figure 2: XPS analysis results of as-prepared a) D and b) D/M samples.

3.1.2 UV-vis analysis

UV-visible (UV-VIS) spectrum of the $CaTiO_3$/NiO and $SrFe_{12}O_{19}$/NiO samples is shown in Figure 3a. Figure 3b depicted the optical band gap of the samples. The optical bandgap of D and $SrFe_{12}O_{19}$/NiO samples is determined using the relation [26]:

$$(\alpha h\nu)^n = A(h\nu - E_g) \quad (1)$$

Whereas A, α, h,ν, and Eg depicted the proportionality constant, absorption coefficient, Planck's constant, frequency of light, and optical bandgap respectively.

The extrapolation of the curves was evaluated to find out the bandgap energy of $CaTiO_3$/NiO and $SrFe_{12}O_{19}$/NiO samples. Figure 3b shows the $(\alpha h\nu)^n$ versus hνas for the evaluation of the bandgap energy. At

shorter wavelengths, the absorptions of light from the $CaTiO_3$/NiO and $SrFe_{12}O_{19}$/NiO samples were found to be high, but at higher wavelengths, they were found to be low (above 360 nm). $SrFe_{12}O_{19}$/NiO sample shows smooth response after decreasing whereas D sample further shows decreasing response after 700 nm. The calculated bandgap for $CaTiO_3$/NiO, and $SrFe_{12}O_{19}$/NiO is 3.31 eV and 3.56 eV respectively. The direct bandgap was found higher for $SrFe_{12}O_{19}$/NiO sample as compared to $CaTiO_3$/NiO sample.

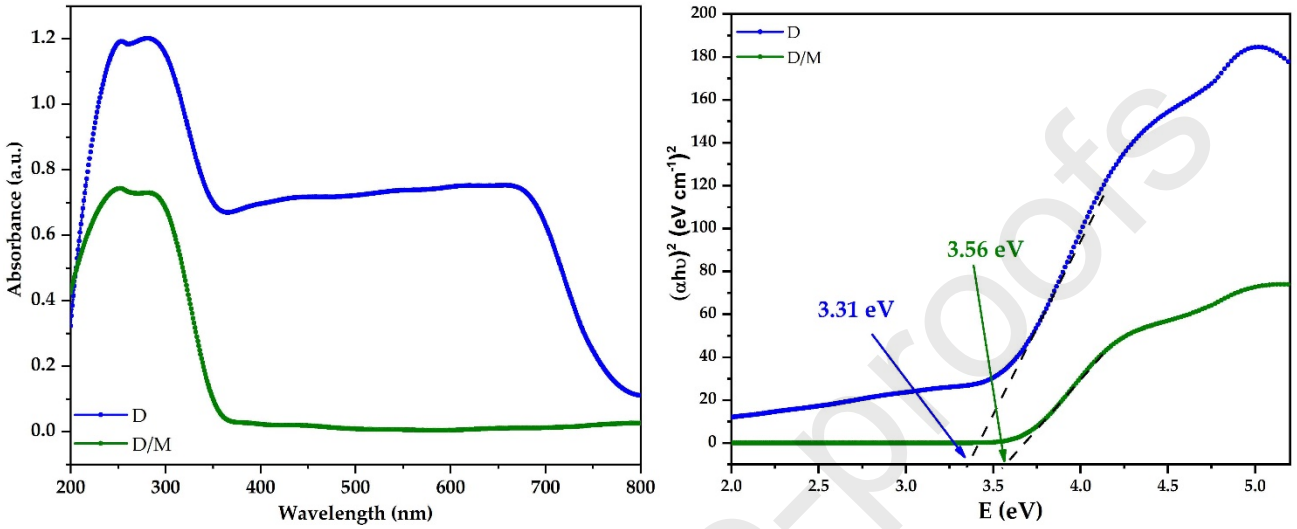

(a) (b)

Fig. 3: (a) The light absorptions and (b) energy bandgaps of D and D/M samples.

3.1.3 FESEM analysis

Figure 4 (a,b) shows the FESEM images of pure $CaTiO_3$ and pure $SrFe_{12}O_{19}$ respectively. The morphology of the pure CaTiO3 shows the rectangular shape particles whereas hexagonal shape of SrFe12O19 ferrites can be easily observed. More porous structure of $CaTiO_3$ was observed whereas well organized and homogenous structure of hexagonal shapes were observed as shown in Figure 3(a,b). Figure 4(c,d) depicts the FESEM images of $CaTiO_3$/NiO sample which is composed of $CaTiO_3$ and NiO powders, from which one can obviously see that the micro cubes of calcium titanate powder have length (1.5 µm) and width (0.4 µm) respectively. The microcubes are well decorated with spherical NiO nanoparticles. The size is in the range of 20-40 nm. Moreover, the surfaces of the calcium titanate micro cubes are appeared to be rough. In Figure 4(e,f), it is observed that polygonal strontium hexaferrite shape nanoparticles, with an diameter of 150-200 nm are completely decorated with NiO nanoparticles and the rough surface of the particles is clearly observed when the magnification is further increased.

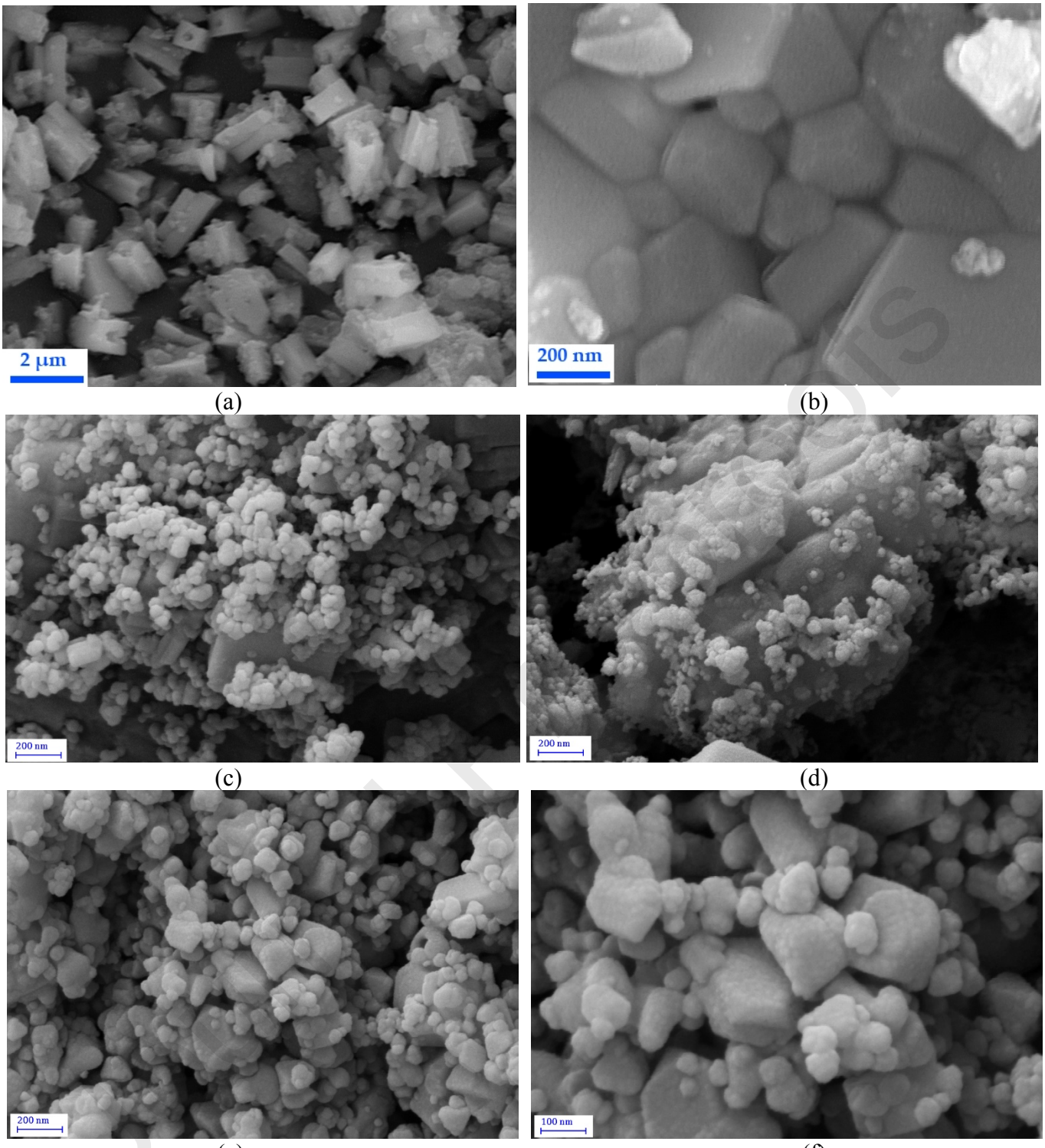

Figure 4: FESEM images of, a) pure $CaTiO_3$, b) pure $SrFe_{12}O_{19}$, c,d) D and e,f) D/M samples.

3.1.4 EDS analysis

Figure 5 (a, b) demonstrates the EDS elemental mapping of $CaTiO_3$/NiO and $SrFe_{12}O_{19}$/NiO samples which confirmed the homogeneous dispersal of element in both samples. The results reveal that Ni element homogenously distribute on the surface of the $CaTiO_3$ and $SrFe_{12}O_{19}$ particles.

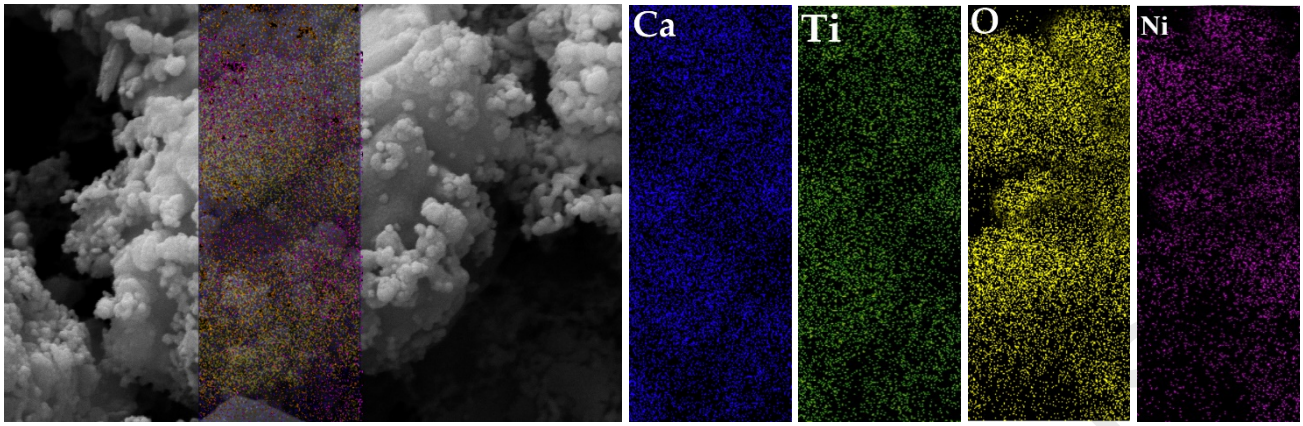

(a)

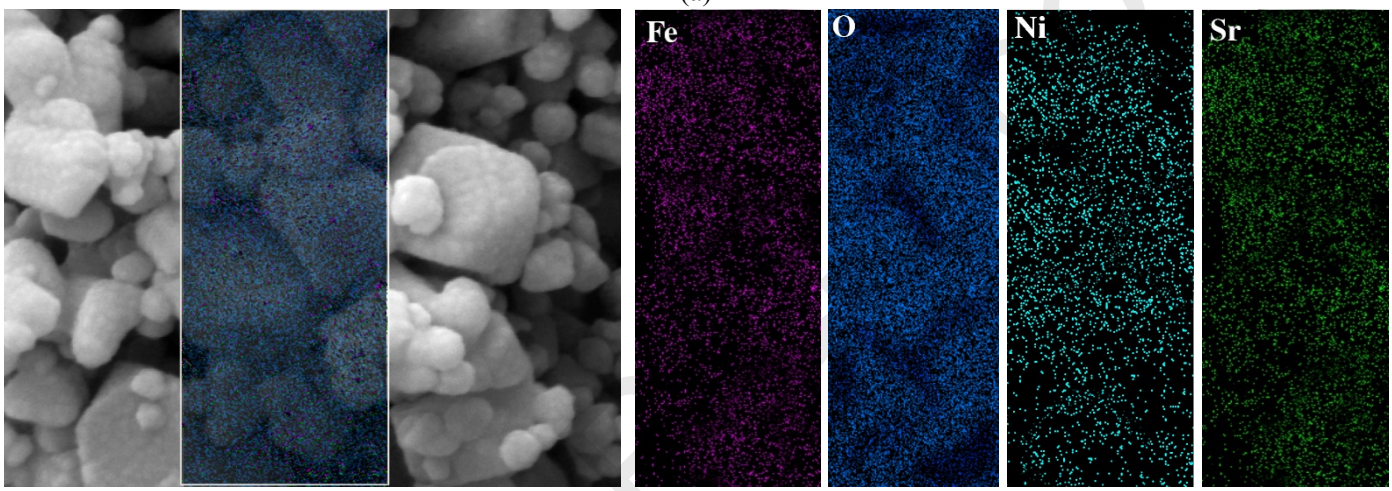

(b)

Figure 5: Elemental mapping analaysis of a) D and b) D/M samples.

3.1.5 BET analysis

Figure 6 (a-d) depicts the N_2 adsorption/desorption isotherms and pore-size diamatere distribution of $CaTiO_3$/NiO and $SrFe_{12}O_{19}$/NiO. Figure 6a shows the N_2 adsorption-desorption isotherms whereas pore-size distribution curve of D sample is depicted in Figure 6b. Similarly, for the $SrFe_{12}O_{19}$/NiO sample the nitrogen adsorption-desorption isotherms are presented in Figure 6c whereas pore-size distribution curve is depicted in Figure 6d.

Surface area of both $CaTiO_3$/NiO and $SrFe_{12}O_{19}$/NiO samples was calculated using BET method, it showed that the specific surface area of $CaTiO_3$/NiO sample is 30.1 m2/g which is the 2.8 times higher than the $CaTiO_3$ prepared by microwave heating method [27]. However, the specific surface area of $SrFe_{12}O_{19}$/NiO sample is 14.3 m2/g which is less than the specific surface area of D sample.

BJH technique was used to calculate the pore volume. To compute the total pore volume and mean pore diameter, the desorption isotherm data was employed. The 0.2 cm3/g of total pore volume and 30 nm of mean

pore diameter was investigated for $CaTiO_3$/NiO sample. In addition, the total pore volume of $SrFe_{12}O_{19}$/NiO sample was 0.2 cm3/g with the mean pore diameter of 14 nm respectively. The H2 type is represented by the provided adsorption-desorption isotherm, whereas the adsorption isotherm depicted the type II isotherm curve for the $CaTiO_3$/NiO and $SrFe_{12}O_{19}$/NiO samples [28].

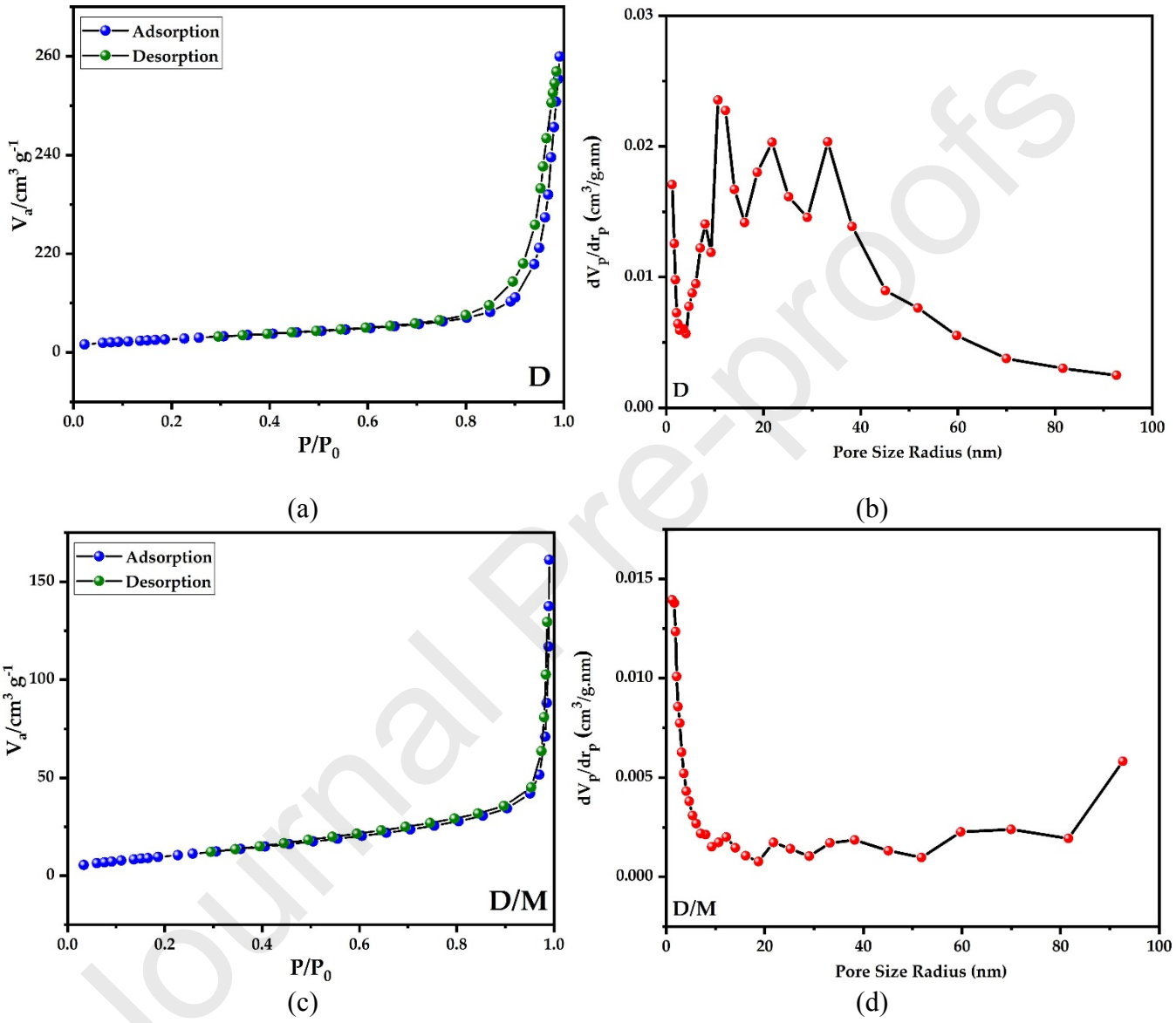

Fig. 6: a) Isotherms of N_2 adsorption-desorption and b) distribution curve of pore-size of D and D/M samples.

3.2 Electromagnetic performances of single and bilayer absorbers

3.2.1 Electromagnetic parameters of Single layer absorber

Figure 7 depicted the frequency dependence of the two EM parameters governing the attenuation of the microwave signal inside our samples, namely the complex ε and μ . The ε′ is shown in Figure 7(a). It is higher for the $CaTiO_3$/NiO sample; this can be easily explained by the fact that $CaTiO_3$/NiO sample contains $CaTiO_3$ instead of $SrFe_{12}O_{19}$ hexaferrite particles. $CaTiO_3$ is reported having a dielectric constant of the order of 100 [29], while for hexaferrite it is around 20 [22]. Hence including either $CaTiO_3$ or $SrFe_{12}O_{19}$ hexaferrite has a different impact on the dielectric constant of the resulting composite powder. As well the imaginary part of the permittivity ε′′ (Figure 7(b)), which is correlated to dielectric loss tangent factor (Figure 7(d)), is higher for $CaTiO_3$/NiO than for $SrFe_{12}O_{19}$/NiO sample due to higher losses of $CaTiO_3$ observed when comparing values reported in [22] and [29]. Finally Figure 7(c) shows the complex magnetic permeability; the μ′ is close to 1.1, and the μ′′ close to 0, in accordance with values given in [22].

It is worth to be mentioned that in multiphase systems such as calcium titanate or $SrFe_{12}O_{19}$ covered by NiO, interfacial polarisation occurs, which participates to the absorption mechanism. As explained in [32], Charges collected at interfaces will generate space charge polarization, according to Maxwell-Wagner Sillars theory. When compared to single phase materials, interfacial polarizations in composites improve the ε_r and $\tan\delta_\varepsilon$ of the material. [33].

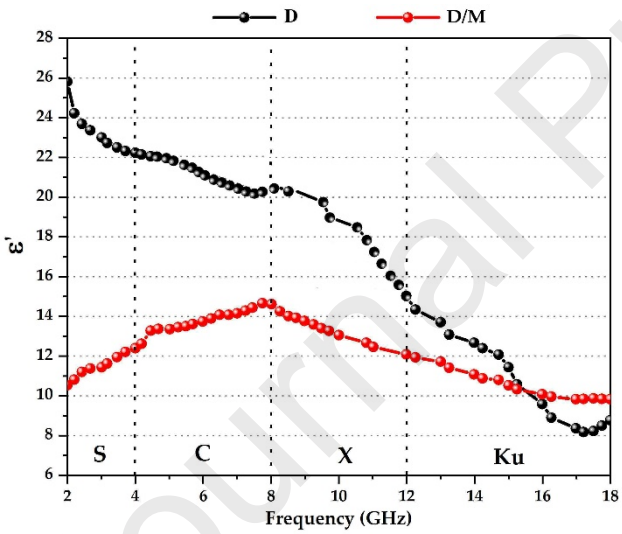

(a)

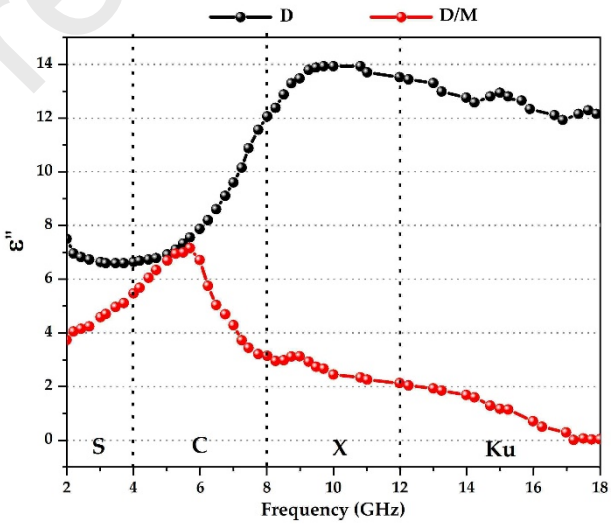

(b)

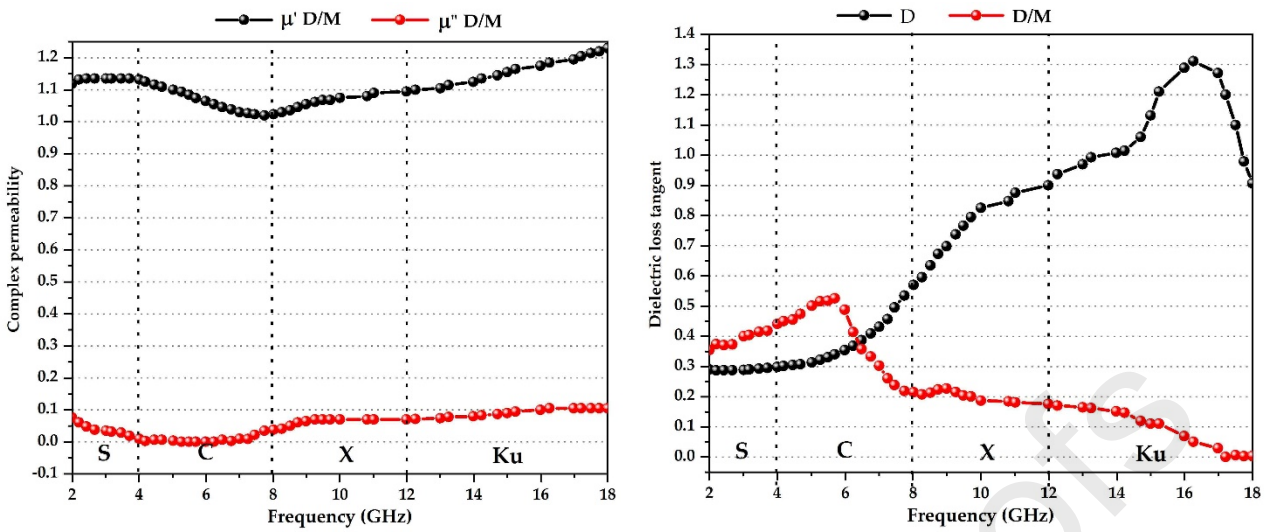

(c) (d)

Figure 7: a) ε′, b) ε″, c) μ_r and d) tan δ_ε of samples in 2-18 GHz.

3.2.2 Microwave attenuation capability of single layer structures

As done in our previous work [1] and recalled here for sake of clarity, the microwave attenuation ability of the samples is investigated by return losses (*RL*) associated to Salisbury configuration, i.e. when the sample is supported by a metal plate that simulates radar functioning The Salisbury setup assesses a material's attenuation capability: if *RL* is minimal, virtually all signal is attenuated inside the sample by absorption, leaving almost none reflected. The input impedance Z_{in} determines the reflection coefficient at the input interface of an absorber in a Salisbury setup. [30]:

$$RL = 20\ log_{10}\left(\frac{Z_{in} - Z_0}{Z_{in} + Z_0}\right) \quad (2)$$

$$Z_{in} = \sqrt{\frac{\mu}{\varepsilon}}\ Z_o\ tanh(\gamma\ d\ ) \quad (3)$$

where $$\gamma = j\ 2\ \pi\ f \sqrt{\varepsilon\ (1 - j\ \tan\delta_\varepsilon)\ \mu\ (1 - j\ tan\delta_\mu)}/c_0 \quad (4)$$

$$d = n\frac{\lambda}{4} = n\ C_0/(4\ f\sqrt{\varepsilon\mu}) \ \rightarrow\ f_0 = n\ c_o/(d\ 4\ \sqrt{\varepsilon\mu}) \quad (5)$$

Z_o is 377 Ohms, d is the thickness, f is the frequency, and tanδ_ε, tanδ_μ ε, μ, are loss tangent factors, permittivity, and permeability respectively. For $CaTiO_3$/NiO sample μ is equal to unity since it contains no magnetic parameters. When the imaginary portion of Z_{in} cancels, *RL* is minimal, and therefore the absorption is highest, as shown in equation (2): When the sample thickness is a multiple of λ/4, i.e. at particular frequencies f_0, this occurs.

Figure 8 illustrates very well equation (4). It is obtained when introducing measured values for ε and μ into equation (2) and varying the values of d from 0.5 mm to 2.5 mm. For the two samples the *RL* curves shown in

Figure 8 (a, b) exhibit a minimum at a frequency that depends on thickness *d*. The higher *d* the lower the frequency f_o. Surprisingly, the frequencies where *RL* is minimum look similar for the two kinds of samples i.e. 6.5 GHz for $d = 2.5$ mm and 8 GHz for $d = 2.0$ mm. This is explained by the fact that the product ε μ is roughly similar for the two samples in this frequency range, i.e. 20 for $CaTiO_3$/NiO sample and 18 for $SrFe_{12}O_{19}$/NiO sample.

Meanwhile the *RL* value differs significantly for the two samples, being higher for $SrFe_{12}O_{19}$/NiO sample. This is correlated with the behavior of the magnitude of the ratio Z_{in}/Z_o shown in Figure 8 (c, d). The *RL* value is minimal when the ratio is closest to 1, i.e. Z_{in} closest to Z_o. For $CaTiO_3$/NiO sample the ratio never reaches unity, while for $SrFe_{12}O_{19}$/NiO sample the curve of the ratio crosses the unit bar at two frequencies for thicknesses $d = 2.5$, 2, and 1.5 mm, and *RL* is minimum between these frequencies.

A good absorber is characterized by *RL* inferior to – 10 d B. This criterion is matched only for $d = 2.5$ mm in the case of $CaTiO_3$/NiO sample, while it is reached for three thicknesses, $d = 2.5$, 2, and 1.5 mm in the case of $SrFe_{12}O_{19}$/NiO sample. The – 10 dB bandwidth is about 1GHz for sample $CaTiO_3$/NiO, while it ranges from 1 GHz to 4 GHz for $SrFe_{12}O_{19}$/NiO sample.

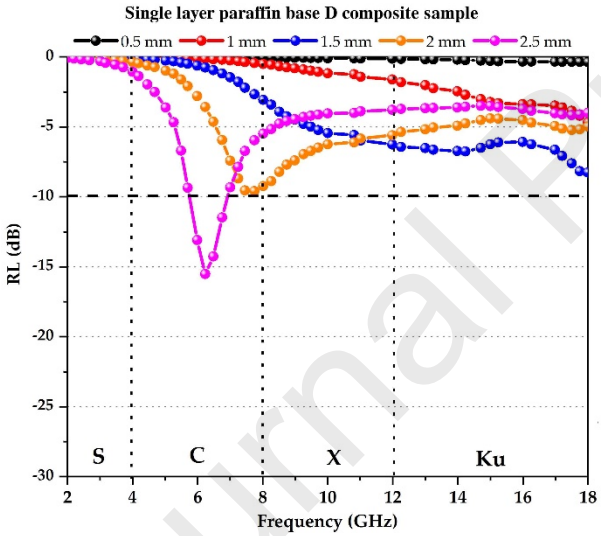

(a)

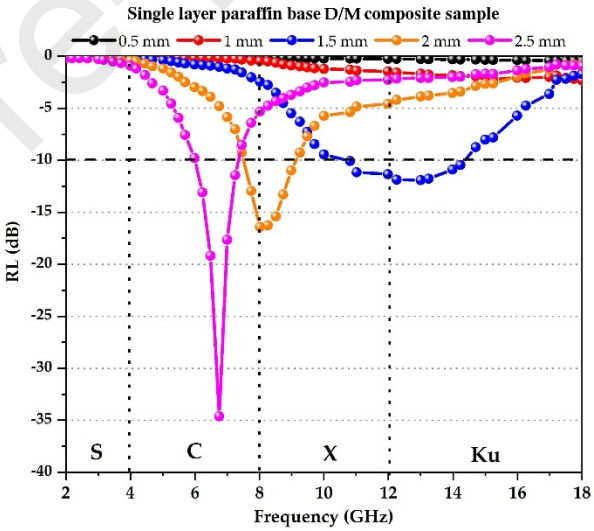

(b)

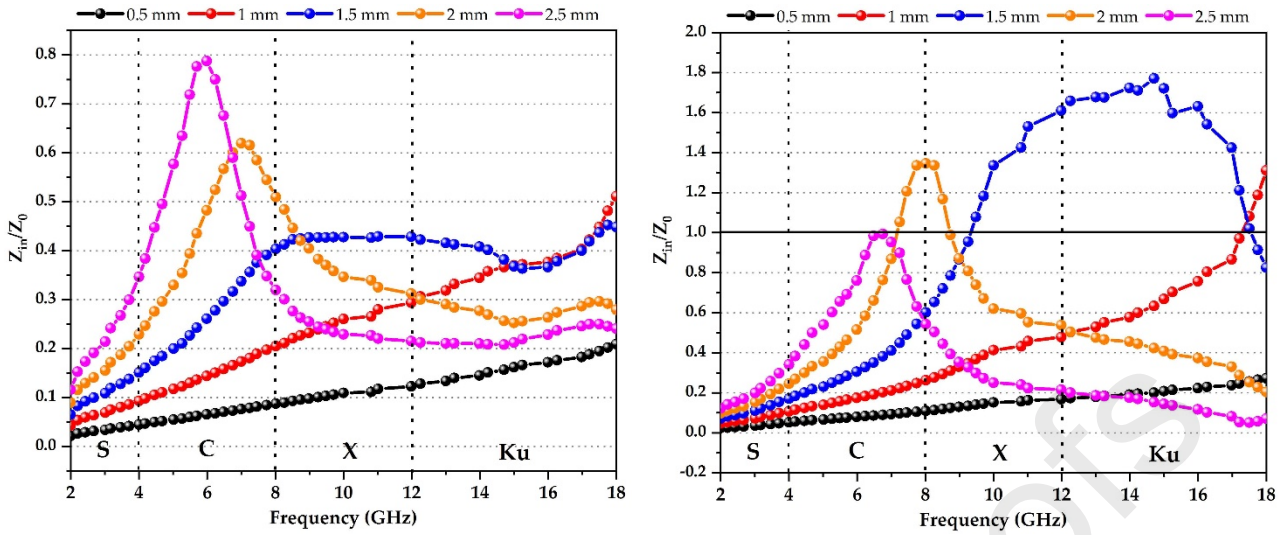

Figure 8. a,b) RL curves, c,d) impedance matching ratio, e) C_0 and f) α of single layer samples.

The signal reflected by the metallic target returns to the input of the absorber with a 180° phase shift at frequency f_0 given by expression (5), while being almost completely attenuated by lossy material absorption, as measured by the attenuation constant $\alpha = Re(\gamma)$ provided by equation (6) and shown in Figure 9(a), resulting in Z_{in} becoming a real number proportional to the material losses. As expected from equation (6) α increases as following the increase of dielectric and magnetic losses shown in Figure 7(c, d).

$$\alpha = \frac{2\pi}{c}\sqrt{2\mu'\varepsilon'}\sqrt{\frac{\mu''\varepsilon''}{\mu'\varepsilon'} - 1 + \sqrt{\left(\frac{\mu''}{\mu'}\right)^2 + \left(\frac{\varepsilon''}{\varepsilon'}\right)^2 + \left(\frac{\mu''\varepsilon''}{\mu'\varepsilon'}\right)^2 + 1}} \quad (6)$$

While, eddy current loss coefficient C_o is shown in Figure 9(b) and defined by equation (7)

$$C_0 = \mu''\mu'^{-2} f^{-1} = 2\pi\mu_0\sigma d^2 \quad (7)$$

For $CaTiO_3$/NiO sample C_o is close to zero since it contains no magnetic material so that μ' = 1 and μ'' is equal to zero. While for $SrFe_{12}O_{19}$/NiO sample C_o is significantly higher than zero, since μ'' > 0 in Figure 7(e)), and is almost constant with frequency from C to Ku band. The magnetic loss is generally known to be caused by the eddy current loss phenomenon, therefore to reduce the effect the values of C_0 must be constant with the frequency [15]. This is indeed verified in Figure 9(b).

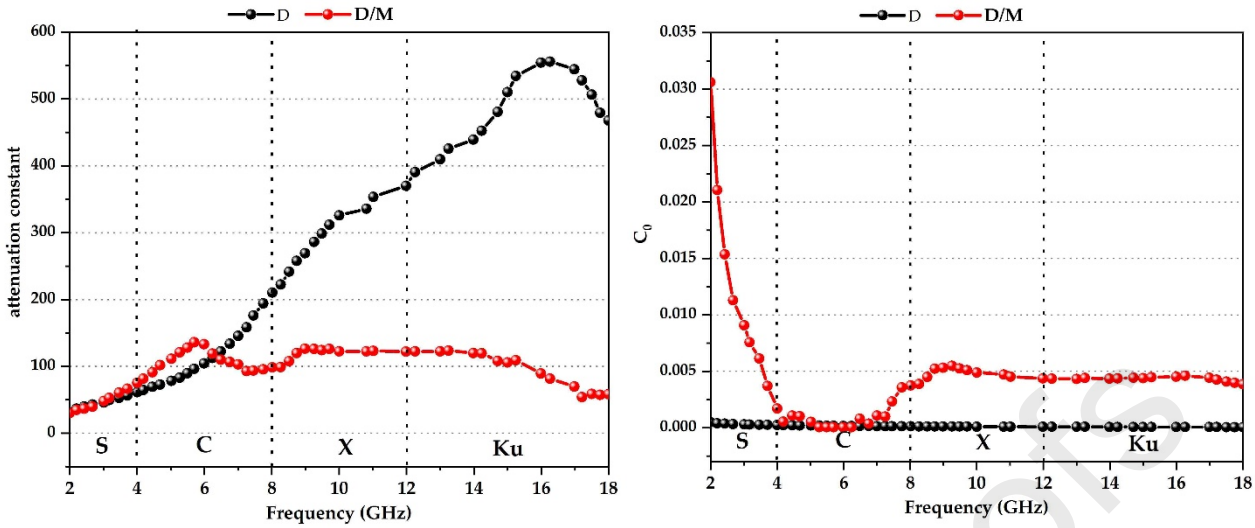

Figure 9. a) attenuation constant of single layer samples. b) eddy current loss factor C_o.

3.2.3 Microwave attenuation capability of bilayer structures

Based on $CaTiO_3$/NiO and $SrFe_{12}O_{19}$/NiO samples, we can investigate their combination in bilayer structures. We consider two configurations; the first one uses $CaTiO_3$/NiO sample as upper layer stacked with $SrFe_{12}O_{19}$/NiO sample as bottom lower layer backed by a reflecting metallic plane in order to reproduce the RCS arrangement, the signal being incident to $SrFe_{12}O_{19}$/NiO sample. In the second configuration the positions of $CaTiO_3$/NiO and $SrFe_{12}O_{19}$/NiO samples are reverted in the bilayer structure, and signal is incident to $SrFe_{12}O_{19}$/NiO sample. Figure 10(a) shows *RL* curves calculated using CST software for the first configuration, while Figure 10(b) corresponds to the second configuration. It can be firstly noted that *RL* values are lower and - 10 dB bandwidth higher for the first configuration, whatever are the respective thicknesses of $CaTiO_3$/NiO and $SrFe_{12}O_{19}$/NiO samples in the bilayer. This behavior is easily explained by the fact that the losses in $CaTiO_3$/NiO sample are much higher than for $SrFe_{12}O_{19}$/NiO sample. As $CaTiO_3$/NiO sample is placed at input of the bilayer, the absorption of the signal in the bilayer is favored. The $SrFe_{12}O_{19}$/NiO sample thus acts as an absorbing layer. Configuration 2 shown in Figure 8(b) fails to match the – 10 dB criterion in a significant bandwidth, since 10 dB bandwidth ranges over 1.5 GHz only for respective thickness 1.5 and 0.5 mm for $CaTiO_3$/NiO and $SrFe_{12}O_{19}$/NiO sample. The two other combinations of thickness 1 mm + 1mm and 0.5 mm + 1.5 mm do not allow to reach *RL* < - 10 dB. Contrarily, for the first configuration the three combinations of thickness, namely 0.5 + 1.5, 1 + 1 and 1.5 + 0.5 mm allow to achieve *RL* below – 10 dB. In particular combination 0.5 mm for D sample and 1.5 mm for $SrFe_{12}O_{19}$/NiO sample yields *RL* around – 10 dB over an exceptional bandwidth of roughly 8 GHz, i.e. from 8 to 16 GHz; while for the two other combinations of thicknesses bandwidths are 2 and 3 GHz.

3.2.3 Comparison of monolayer and bilayer structures

Here we compare the minimal *RL* values obtained for monolayers and bilayer configurations, and for the same total thickness, namely 2 mm. For $CaTiO_3$/NiO sample RL_{min} = - 10 dB, for $SrFe_{12}O_{19}$/NiO sample RL_{min} = - 16.5 d B and for configuration 1 of bilayer RL_{min} = - 32 dB, for combination 1 + 1 mm.

This allows us to conclude on the superiority of bilayer configuration in terms of reflectivity and bandwidth. The bilayer structure allows to tune the bandwidth and the reflectivity by changing the thickness and the order of the stacking of each layer.

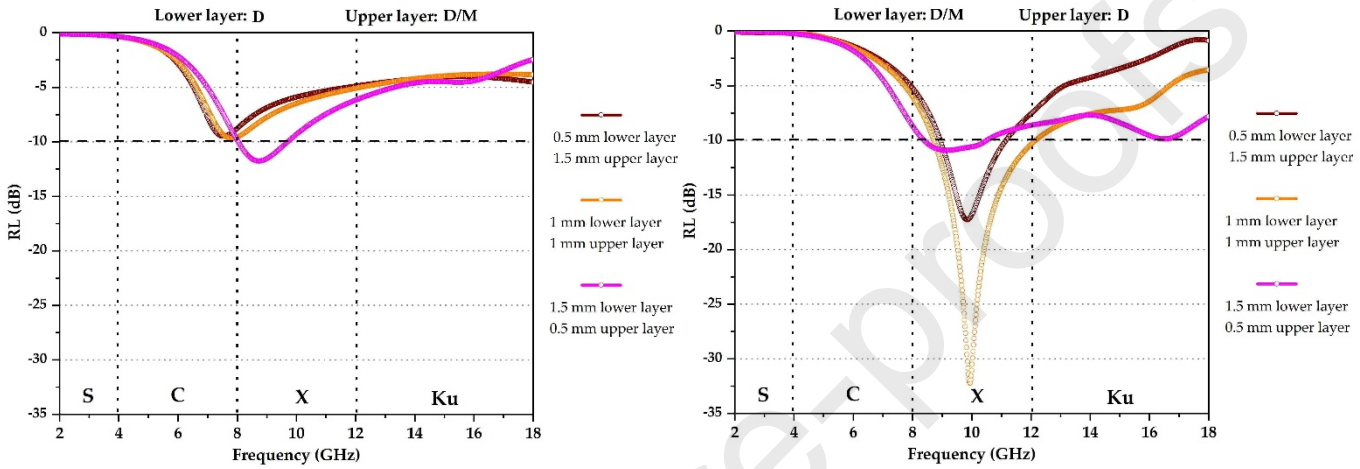

(a) (b)

Figure 10. Simulated *RL* curves of bi- layer absorber with total thickness of 2 mm. (a) configuration 1: upper layer D, lower layer D/M (b) configuration 2: upper layer D/M, lower layer D.

Table 1 summarizes the performances for monolayer and bilayer configurations. In view of this we define: Table 1 shows that in terms of figure of merit (FOM), two bilayer samples, highlighted in bold type, stand out. Their thicknesses are 1 mm top/1 mm bottom and 1.5 mm top/0.5 mm bottom, respectively. Both fractional bandwidth (FB) and |RL| are greater than most other samples, explaining their superiority.

Table 1. Comparison of dissipation performances for absorber samples with reflection loss lower than - 10 d B

Sample	thickness (mm)	Fo (GHz)	BW (GHz)	|RL| (dB)	FB (%)	FOM
Monolayer D	2.5	6.2	1.3	16	21	336
Monolayer M/D	1.5	13	4	13	31	403
Monolayer M/D	2.0	8.2	2.5	17	30	510
Monolayer M/D	2.5	6.8	1.3	35	19	665
Bilayer D + D/M	0.5 + 1.5	9.8	2	17.5	20	350
Bilayer D + D/M	**1 + 1**	**10**	**3**	**33**	**30**	**990**
Bilayer D + D/M	**1.5 + 0.5**	**12**	**8**	**10**	**67**	**670**
Bilayer D/M + D	1.5 + 0.5	9	1.5	13	17	221

3.2.4 Measured electromagnetic parameters of optimal bilayer absorbers

Figure 11 (a-f) shows the electromagnetic parameters of fabricated bilayer absorbers having optimum thicknesses determined from results presented in Figure 10. The bilayer absorber is composed of different orientation of the upper layer and lower layers of $SrFe_{12}O_{19}$/NiO and $CaTiO_3$/NiO with having each a 1 mm thickness. The real and complex permittivity values of configuration having lower layer $CaTiO_3$/NiO and upper layer $SrFe_{12}O_{19}$/NiO was lower as compared to configuration upper layer $CaTiO_3$/NiO and lower layer of $SrFe_{12}O_{19}$/NiO. The permittivity response was higher in C band whereas it decreased in X and Ku bands as shown in Figure 11 (a,b). The real and complex permeability response of lower layer $CaTiO_3$/NiO and upper layer $SrFe_{12}O_{19}$/NiO absorbers was higher as compared to upper layer $CaTiO_3$/NiO and lower layer of $SrFe_{12}O_{19}$/NiO absorbers. However, permeability response was lower in C band and almost smooth response in X and Ku band as depicted in Figures 11 (c,d). The dielectric response of lower layer $CaTiO_3$/NiO and upper layer $SrFe_{12}O_{19}$/NiO absorbers was higher as compared to upper layer $CaTiO_3$/NiO and lower layer of $SrFe_{12}O_{19}$/NiO absorbers. However, the magnetic response of upper layer $CaTiO_3$/NiO and lower layer of $SrFe_{12}O_{19}$/NiO absorbers was lower as compared to lower layer $CaTiO_3$/NiO and upper layer $SrFe_{12}O_{19}$/NiO absorbers. This demonstrates the significance of the bottom and upper layer orientations in absorbers.

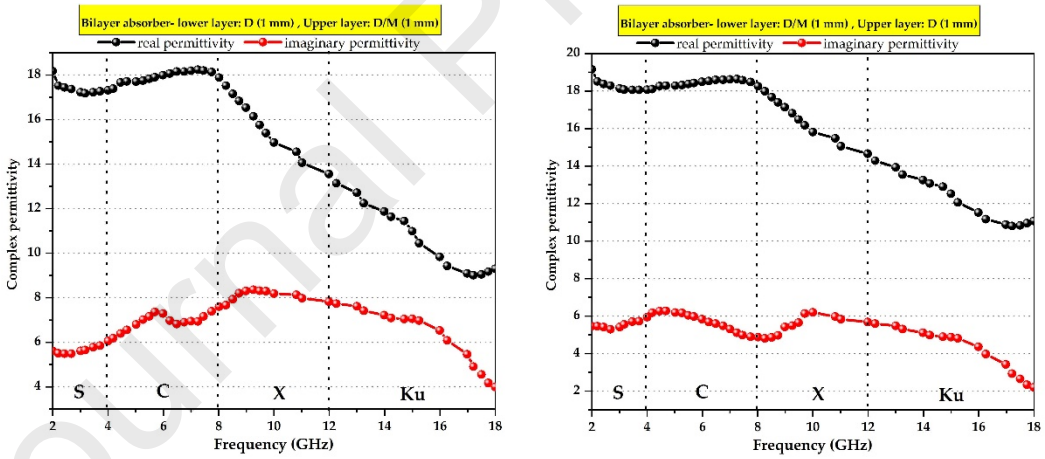

(a) (b)

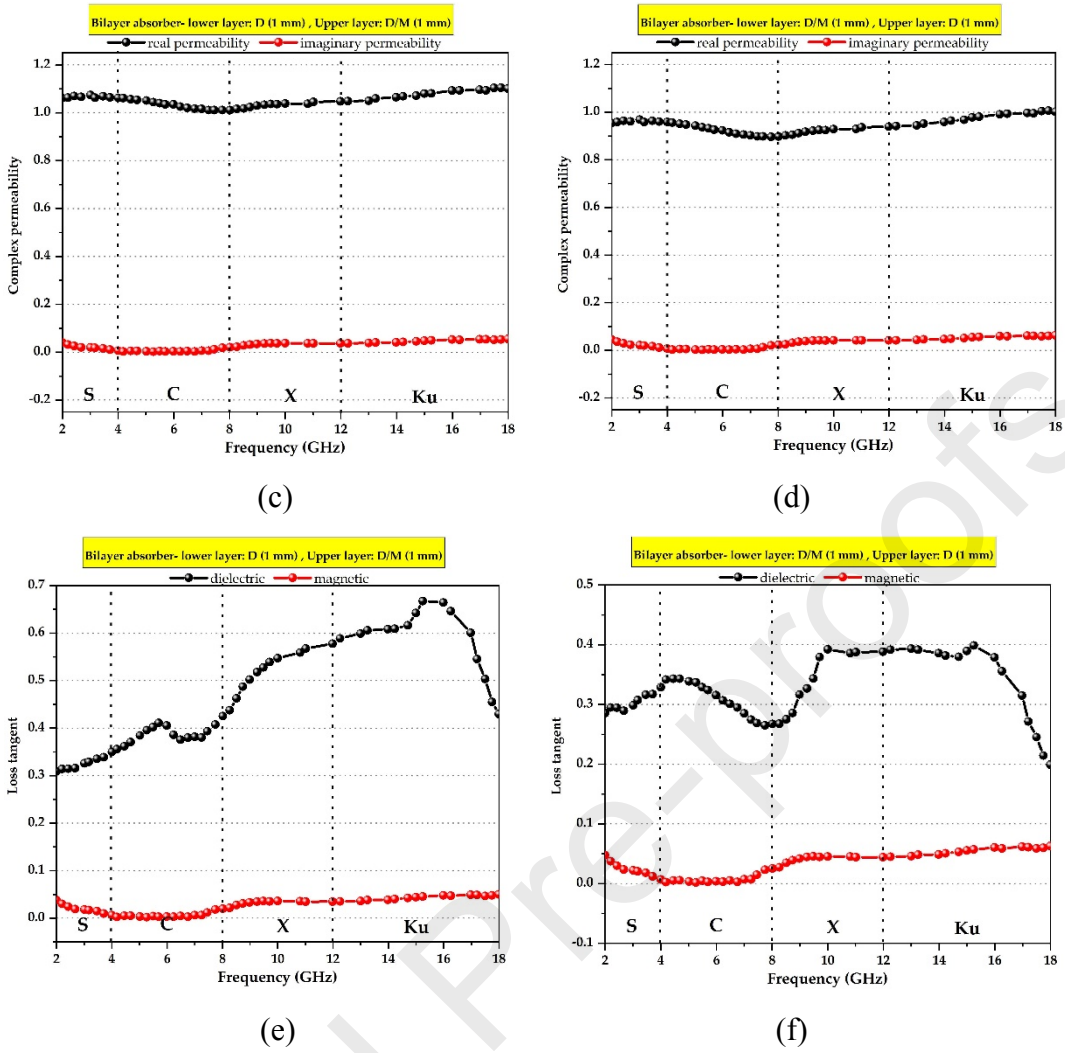

Fig. 11: Electromagnetic parameters: a,b) complex permittivity, c,d) complex permeability and e,f) loss tangents of as-prepared bilayer absorbers with optimum thicknesses of each layers.

3.2.5 Microwave absorption capability of fabricated optimal bilayer absorbers

Figures 12 (a-c) shows the simulation of reflection loss curves, impedance matching ratio and α of as-prepared double layer absorbers with optimum thickness of each layer. The RL value in bilayer sample in which $CaTiO_3$/NiO composite powder placed at absorbing layer and $SrFe_{12}O_{19}$/NiO composite powder placed at matching layer was lower as compared to bilayer absorber in which these composites are placed at reverse situation. The lower layer $CaTiO_3$/NiO and upper layer $SrFe_{12}O_{19}$/NiO absorber shows lower RL response -33 dB whereas lower layer of $SrFe_{12}O_{19}$/NiO and upper layer $CaTiO_3$/NiO absorber depicted -17 dB respectively. Both absorbers show RL response in C band region. Z_{in}/Z_o response from the lower layer $CaTiO_3$/NiO and upper layer $SrFe_{12}O_{19}$/NiO absorbers was also lower as compared to lower layer of $SrFe_{12}O_{19}$/NiO and upper layer $CaTiO_3$/NiO absorber. In addition, the attenuation constant of the lower layer $CaTiO_3$/NiO and upper

layer $SrFe_{12}O_{19}$/NiO absorbers is higher as compared to lower layer of $SrFe_{12}O_{19}$/NiO and upper layer $CaTiO_3$/NiO absorber. Both the absorbers show higher response in Ku band.

The two-layer absorbers with 2 mm thickness display accurate RL values, but not the frequency monitored in the simulation process. In reality, it's possible that this discrepancy was created by a mistake in the preparation procedure.

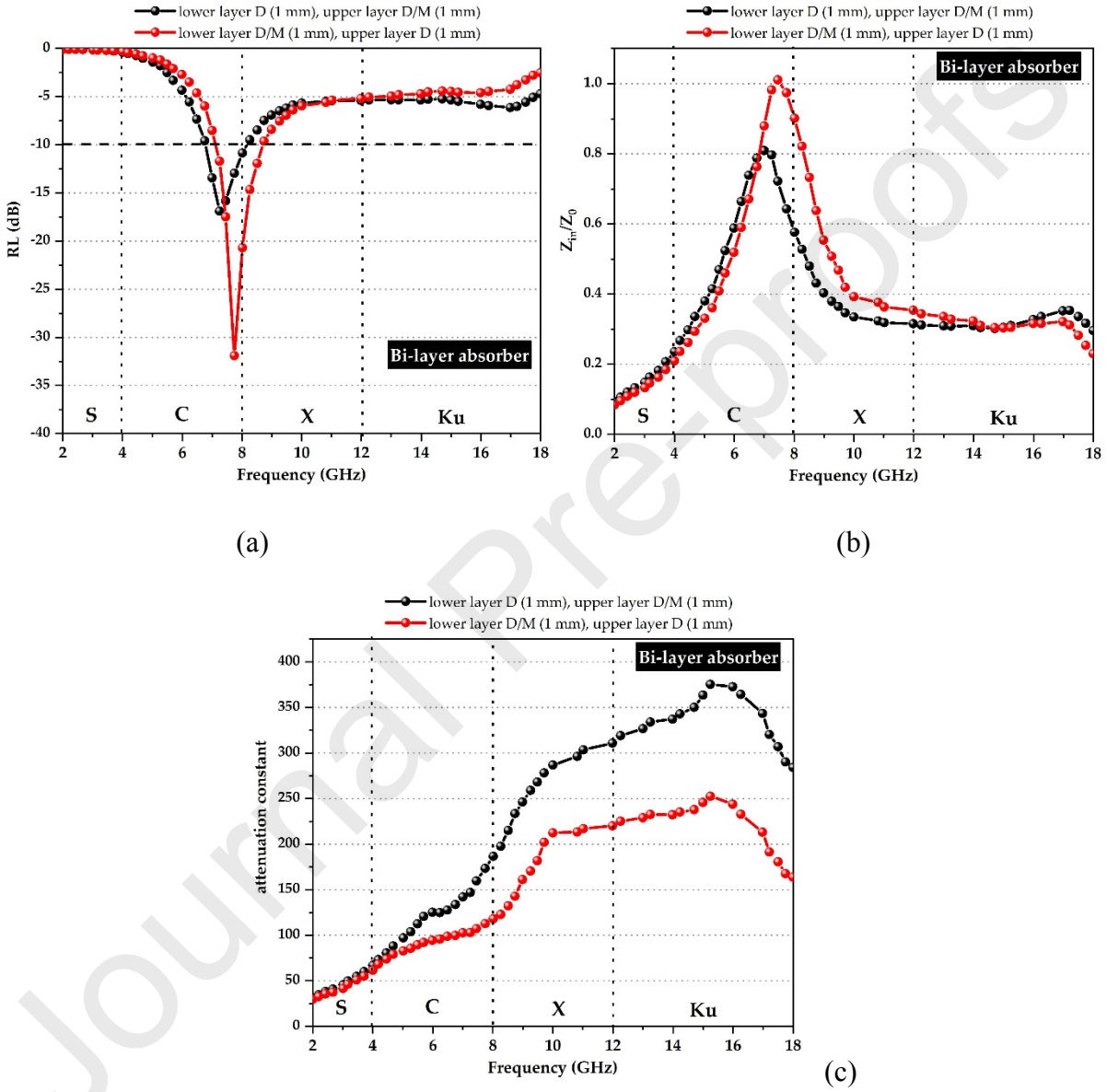

Fig. 12. a) reflection loss curves, b) $|Z_{in}/Z_0|$ and c) attenuation constant of as-prepared double layer absorbers with optimum thickness of each layer.

3.2.6 Comparison with state-of-the art

Table 2 compares our best result obtained in Table 1 and Figure 10 with absorbers presented in the literature and involving calcium titanate and/or strontium-based hexaferrites. We conclude that our absorber is amongst the best in terms of FOM_N (normalized FOM), since only three structures of absorbers marked in italic font and reported in references [21,22,31] outperform the characteristics of our best absorber reported in Table 1.

Table 2. Comparison of performances with state-of-the art

Reference	Structure/ material	fo [GHz]	D (mm)	RL (dB)	BW (GHz)	FBW (%)	FOM_D
17	CaTiO3 in epoxy	8.5	1	30	2.2	25.9	6851
18	CaTiO3 in epoxy	10.5	2.8	14	3	28.6	4081
19	SrFe hexa in epoxy	10.21	3	39.6	3.36	32.9	12763
20	SrFe12O19 in epoxy	13.6	3.5	28.6	1	6.75	1219
21	***Sr hexaferrite+ zinc ferrite***	*8.6*	*2.2*	*37*	*3*	*34.88*	***20465***
22	***rGO/Sr ferrite in polyaniline***	*16.08*	*1.5*	*45*	*5.48*	*34.*	***19074***
31	***Epoxy/[CaTiO3 + $ZnFe_2O_4$] bilayered configuration***	*9.2*	*0.5/1.5*	*24*	*4.5*	*48.9*	***18342***
32	Fe3O.0.5BaTiO300.5 In paraffin	14.6	1.7	48	3.5	23.97	13908
Our work	**See table 1**	**12**	**1+1**	**33**	**3**	**30**	**14850**

FOM: the figure of merit, **D**: Thickness, **fo**: the absorption center frequency, **BW**: bandwidth, **FBW**: fractional bandwidth

4. Conclusions

In this paper we successfully synthesized via hydrothermal method two distinct nanocomposites of $CaTiO_3$ micro-cubes (denoted D sample) and polygonal $SrFe_{12}O_{19}$ (denoted D/M sample), both decorated with NiO nanoparticles. The physico-chemical features of as-prepared samples were evaluated via XRD, XPS and FSEM analysis.

XRD patterns of each sample reveal the presence two distinct phases. In addition to the characteristic peaks of $CaTiO_3$ and $SrFe_{12}O_{19}$ in D and D/M samples respectively, new broad diffraction peaks were observed which related to pure NiO nanoparticles present on both $CaTiO_3$ and $SrFe_{12}O_{19}$ particles. Moreover, for $SrFe_{12}O_{19}$ phase, all characteristic peaks were assigned to their crystal planes and there were no impurity peaks.

The XPS analysis of $CaTiO_3$/NiO sample clearly illustrate the presence of C, Ca, Ti, O and Ni elements. While Sr3d, C1s, O1s, Fe2p and Ni2p peaks were observed for D/M sample. Also both spectras confirm the formation of nickel oxide phase in both samples.

The FESEM images of $CaTiO_3$/NiO sample clearly show that micro cubes of calcium titanate powder with approximately 1.5 μm in length and 0.4 μm in width are well decorated with spherical NiO nanoparticles witqth size in the range of 20-40 nm having rough surface. While for D/M sample polygonal shape $SrFe_{12}O_{19}$ particles, with an average diameter of 150-200 nm, are completely decorated with NiO nanoparticles having also rough surface.

The EDS elemental mapping of $CaTiO_3$/NiO and D/M samples confirm the homogeneous distribution of element in both samples. The results reveal that Ni element homogenously distribute on the surface of the $CaTiO_3$ and $SrFe_{12}O_{19}$ particles.

The microwave absorption capability is studied in both samples through the evaluation of return losses *RL*. Monolayer and bilayer configurations were evaluated as a function of thickness of paraffin slab loaded with D or D/M powder. For monolayer configuration minimum *RL* is obtained for thickness equal to 2.5 mm, with *RL* = - 17 d B for D sample, and *RL* = -35 d B for D/M sample

Next we simulated bilayer structures by stacking either D sample followed by D/M sample (configuration 1) or reversely D/M sample followed by D sample (configuration 2). Each bilayer configuration has a global thickness equal to 2 mm while thickness of D and D/M slab can be varied inside the stack. Values of *RL* inferior to – 10 dB are obtained for first configuration only. i.e. for stack D/DM. In particular for 1.0+1.0 mm stack, RL = -33 dB, while stack 0.5+1.5 mm stack exhibits *RL* close to – 10 dB over an exceptional 9 GHz bandwidth.

Finally, we fabricated two bilayer structures D/M followed by D and D followed by D/M, each layer having a thickness of 1 mm. Measurements of RL confirm that the first configuration allows to achieve the best value of -35 dB.

As a conclusion the bilayer structure offers better flexibility for the design of efficient microwave absorbers since absorption level and bandwidth can be adjusted varying thickness and order of stacking. Our analysis also shows that our bilayer absorber competes well with the state-of-the art

Acknowledgments

The authors are grateful for the financial support provided by the National Natural Science Foundation of China (No.52000036) and the Science and Technology Planning Project of Guangzhou City (No. 202102021061).

References

[1] Yan Cao, Abdeliazim Mustafa Mohamed, Mehdi Abdollahzadeh, Isabelle Huynen, "Rational Design of CoNi@C-BTC/rGO Nanocomposite Coated with PEDOT Polymer Towards Enhancing the Microwave Absorption in X-band Frequency", Journal of Alloys and Compounds, vol. 862, article n° 158371, January 2021.

[2] Violette, N. Electromagnetic Compatibility Handbook; Springer: Berlin/Heidelberg, Germany 2013

[3] Chambers, B. Optimum design of a Salisbury Screen radar absorber. IEE Electron. Lett. 1994, 30, 1353–1354.

[4] Kim, J.-B. Design of Salisbury screen absorbers using dielectric lossy sheets. In Proceedings of the 2011 IEEE International Conference on Microwave Technology & Computational Electromagnetics, Beijing, China, 22–25 May 2011; pp. 1–2.

[5] Oh, J.-H.; Oh, K.-S.; Kim, C.-G.; Hong, C.-S. Design of radar absorbing structures using glass/epoxy composite containing carbon black in X-band frequency ranges. Compos. Part B 2004, 35, 49–56.

[6] Kim, J.-B.; Lee, S.-W.; Kim, C.-G. Comparison study on the effect of carbon nano materials for single-layer microwave absorbers in X-band. Compos. Sci. Technol. 2008, 68, 2909–2916.

[7] Kim, B. Adv. Compos. Mater. Publisher:City, Country; 2012, 21, 333.

[8] Raj, P.M.; Mishra, D.; Sharma, H.; Swaminathan, S.; Tummala, R. Chap. 1 Nanomagnetic materials and structures, and their applications in integrated rf and power modules. *Nanomagnetism*. 2014; pp. 1–29.

[9] Qin, F.; Peng, H.X.; Pankratov, N.Y.; Phan, M.; Panina, L.V.; Ipatov, M.; Zhukova, V.; Zhukov, A.; Gonzalez, J. Exceptional electromagnetic interference shielding properties of ferromagneticmicrowires enabled polymer composites. *J. Appl. Phys.* **2010**, *108*, 044510.

[10] Ma, X.; Zhang, Q.; Luo, Z.; Lin, X.; Wu, G. A novel structure of ferroaluminum-based sandwich composite for magnetic and electromagnetic interference shielding. *Mater. Des.* **2016**, *89*, 71–77.

[11] Singh, K.; Ohlan, A.; Bakhshi, A.; Dhawan, S. Synthesis of conducting ferromagnetic nanocomposite with improved microwave absorption properties. *Mater. Chem. Phys.* **2010**, *119*, 201–207.

[12] D. Micheli, R. Pastore, A. Vricella, and M. Marchetti, "Matter's electromagnetic signature reproduction by graded-dielectric multilayer assembly," IEEE Microwave Theory and Techn., vol. 65(8) 2801–2809, 2017.

[13] Shital Patangrao Pawar, High frequency millimetre wave absorbers derived from polymeric nanocomposites, Polymer, Vol 84, pp 398–419, 2016

[14] Jean-Michel Thomassin, Polymer/carbon-based composites as electromagnetic interference (EMI) shielding materials, Materials Science and Engineering: R: Reports Vol. 74(7), 211–232, 2013

[15] Fusheng Wen, Fang Zhang, Zhongyuan Liu, "Investigation on Microwave Absorption Properties for Multiwalled Carbon Nanotubes/Fe/Co/Ni Nanopowders as Lightweight Absorbers, "J. Phys. Chem. C,115 (29),14025–14030, 2011.

[16] Zhou Wang and Guang-Lin Zhao, " Electromagnetic wave absorption of multi-walled carbon nanotube–epoxy composites in the R band," J. Mater. Chem. C, 2014, 2, 9406–9411.

[17] M MURUGAN*, V K KOKATE and M S BAPAT, "Synthesis, characterization and evaluation of reflectivity of nanosized CaTiO3/epoxy resin composites in microwave bands", Bull. Mater. Sci., Vol. 34, No. 4, July 2011, pp. 699–704.

[18] Seyyed Salman Seyyed Afghahi, Mojtaba Jafarian, Charalampos A. Stergiou, "Multicomponent nanocomposites with carbonyl Fe-CoFe2O4-CaTiO3 fillers for microwave absorption applications", Materials and Design 112 (2016) 462–468.

[19] Soma Chakraborty, Nidhi Saxena Bhattacharyya, and Satyajib Bhattacharyya, "Single Layered Wide Bandwidth Nanosized Strontium Hexa-Ferrite Filled LLDPE Absorber in X-Band", Progress In Electromagnetics Research B, Vol. 71, 137–152, 2016.

[20] Shenhui Dong, Chucheng Lin, Xianfeng Meng, "One-pot synthesis and microwave absorbing properties of ultrathin SrFe12O19 nanosheets", Journal of Alloys and Compounds 783 (2019) 779e784.

[21] Na Chen, Guohong Mu, Xifeng Pan, Keke Gan, Mingyuan Gu, "Microwave absorption properties of SrFe12O19/ZnFe2O4composite powders", Materials Science and Engineering B 139 (2007) 256–260.

[22] Juhua Luo, Pan Shen, Wei Yao, Cuifeng Jiang and Jianguang Xu, "Synthesis, Characterization, and Microwave Absorption Properties of Reduced Graphene Oxide/Strontium Ferrite/Polyaniline Nanocomposites", Nanoscale Research Letters (2016) 11:141.

[23] Jifu Huang; Ke Wu; P. Morin; C. Akyel, "Characterization of highly dispersive materials using composite coaxial cells: electromagnetic analysis and wideband measurement", IEEE Transactions on Microwave Theory and Techniques, Volume: 44, Issue: 5, May 1996, pp. 770 – 777.

[24] Akhtar, Majid Niaz, Muhammad Yousaf, Yuzheng Lu, Muhammad Azhar Khan, Ali Sarosh, Mina Arshad, Misbah Niamat, Muhammad Farhan, Ayyaz Ahmad, and Muhammad Umar Khallidoon. "Physical, structural, conductive and magneto-optical properties of rare earths (Yb, Gd) doped Ni–Zn spinel nanoferrites for data and energy storage devices." Ceramics International 47, no. 9 (2021): 11878-11886.

[25] Aamir, Muhammad, Waqas Aleem, Majid Niaz Akhtar, Aamir Alaud Din, Ghazala Yasmeen, and Muhammad Naeem Ashiq. "Synthesis and characterizations of Co–Zr doped Ni ferrite/PANI

nanocomposites for photocatalytic methyl orange dye degradation." Physica B: Condensed Matter (2021): 413392.

[26] Yousaf, Muhammad, Yuzheng Lu, Hu Enyi, Baoyuan Wang, Majid Niaz Akhtar, Asma Noor, Muhammad Akbar, MAK Yousaf Shah, Faze Wang, and Bin Zhu. "Tunable Magneto-optical and Interfacial Defects of Nd and Cr-doped Bismuth Ferrite Nanoparticles for Microwave Absorber Applications." Journal of Colloid and Interface Science (2021).

[27] Patil BM, Srinivasa RS, Dharwadkar SR. Synthesis of CaTiO3 from calcium titanyl oxalate hexahydrate (CTO) as precursor employing microwave heating technique. Bull Mater Sci 2007; 30 (3): 225-9.

[28] Sing KSW, Everett DH, Haul RAW, et al. Reporting physisorption data for gas/solid systems with special reference to the determination of surface area and porosity. Pure Appl Chem 1985; 57(4):603-19.

[29] Pavel Ctibora, Jiri Kotlana, Zdenek Pala, Josef Sedlacek, Zuzana Hajkova, Tomas Matys Grygar, "Calcium titanate (CaTiO3) dielectrics prepared by plasma spray and post-deposition thermal treatment", Materials Research Bulletin 72 (2015) 123–132.

[30] Pozar, D. In Microwave Engineering, 2nd ed.; Wiley: New York, NY, USA, 1998.

[31] Wenhui Cai, Marischa Elveny, Majid Niaz Akhtar, "Enhanced X-band wave dissipation performance in bilayer absorber composed of bare epoxy resin and epoxy resin filled with [CaTiO3/ZnFe2O4]@C nanocomposite", Journal of Magnetism and Magnetic Materials, Volume 539, 1 December 2021, 168385.

[32] Yue Huang, Jindou Ji, Yan Chen, Xiang Li, Jun He, Xingwang Cheng, Shuli He, Ying Liu, Jiping Liu, "Broadband microwave absorption of Fe3O4eBaTiO3 composites enhanced by interfacial polarization and impedance matching", Composites Part B, Volume 163, 15 April 2019, Pages 598-605.

[33] Anil Ohlan, Kuldeep Singh, Amita Chandra, and Sundeep K. Dhawan, "Microwave Absorption Behavior of Core-Shell Structured Poly (3,4-EthylenedioxyThiophene)-Barium Ferrite Nanocomposites", Applied Materials and Interfaces, VOL. 2 • NO. 3 • 927–933 • 2010.

Declaration of interests

☒ The authors declare that they have no known competing financial interests or personal relationships that could have appeared to influence the work reported in this paper.

☐The authors declare the following financial interests/personal relationships which may be considered as potential competing interests:

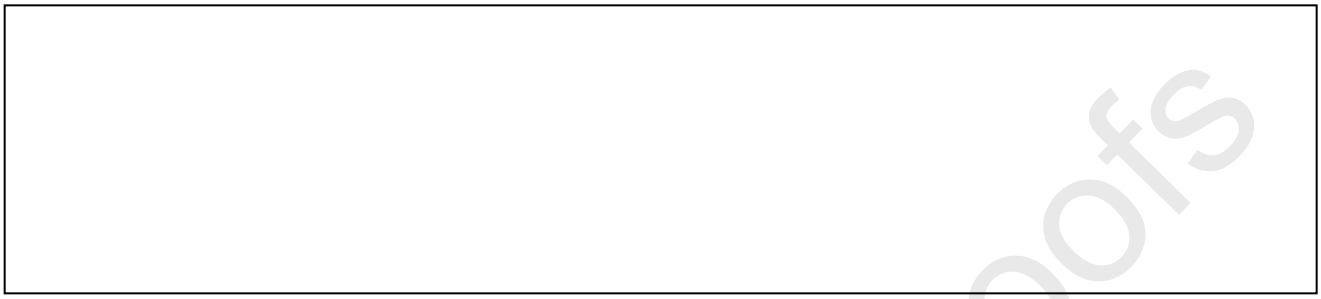

Li Feng[1,*], Jiajun Liu[1], Isabelle Huynen[2], Mustafa Z. Mahmoud[3,4], Majid Niaz Akhtar[5,*]

1- School of Civil and Transportation Engineering, Guangdong University of Technology, Guangzhou 510006, Guangdong, China

2- ICTEAM Institute, ELEN Division, Place du Levant 3, Louvain-la-Neuve B-1348, Belgium

3-Department of Radiology and Medical Imaging, College of Applied Medical Sciences, Prince Sattam bin Abdulaziz University, Al-Kharj 11942, Saudi Arabia

4- Faculty of Health, University of Canberra, Canberra, ACT, Australia.

5- Department of Physics, Muhammad Nawaz Sharif University of Engineering and Technology, Multan 60000 Pakistan

Corresponding authors email:

Majid Niaz Akhtar: majidniazakhtar@mnsuet.edu.pk, majidniazakhtar@gmail.com

Li Feng: fl19860314@126.com